

**Higher-order rogue-wave fission in the presence of self-steepening and Raman self-frequency shift**Amdad Chowdury <sup>1</sup>, Wonkeun Chang,<sup>2</sup> and Marco Battiato<sup>1</sup><sup>1</sup>*School of Physical and Mathematical Sciences, Nanyang Technological University, 637371, Singapore*<sup>2</sup>*School of Electrical and Electronic Engineering, Nanyang Technological University, 639798, Singapore* (Received 21 September 2022; revised 20 March 2023; accepted 21 April 2023; published 10 May 2023)

Using the generalized nonlinear Schrödinger equation, we investigate how the effect of self-steepening and Raman-induced self-frequency shift impact higher-order rogue-wave solutions. We observe that each effect breaks apart the higher-order rogue wave, reducing it to its constituent fundamental parts, in a similar manner to how a higher-order soliton undergoes fission. Applying a local inverse-scattering technique, we show that under the effect of self-frequency shift, the emergence of a rogue wave significantly influences the surrounding wave background, triggering solitons, breathers, and new rogue waves. We demonstrate that under the combined effect of third-order dispersion, self-steepening, and Raman-induced self-frequency shift, the disintegrated elements of higher-order rogue waves become fundamental solitons, creating an asymmetrical spectral profile that generates both red- and blue-shifted frequency components. We also show the intermediary processes of the fission steps prior to soliton transformation which can only be observed in the presence of weak perturbations. These observations reveal the mechanisms that create a large number of solitons in the process of modulation instability-induced supercontinuum generation from a continuous-wave background in optical fibers.

DOI: [10.1103/PhysRevA.107.053507](https://doi.org/10.1103/PhysRevA.107.053507)**I. INTRODUCTION**

The rogue-wave solution of the nonlinear Schrödinger equation (NLSE) is attractive because of its ability to explain sudden extreme formations in nature, such as oceanic rogue waves, light pulses with unusually high intensities, and localized structures in Bose-Einstein condensates. After three decades of intense study, the rogue-wave solution has extended to a range of other multidisciplinary fields from optics [1–14] to economics [15].

Optical rogue waves are short burst of light pulses with high intensities that appear in a chaotic optical wave field. The first observation of the existence of an optical rogue wave was reported in the work of Solli *et al.* in fiber supercontinuum generation [16]. Since then, the phenomenon has been studied in various different branches of optics because of its multiplicity of applications and impact such as in optical cavities [17,18], mode-locked lasers [19,20], photonic crystal fibers [21], Raman fiber lasers and amplifiers [22,23], and optical parametric processes [24]. A comprehensive report on recent progress in the research of optical rogue waves can be found in Refs. [25–27].

Instability seeded by noise acts as a breeding ground for the emergence of optical rogue waves. This is described by a process called modulation instability (MI) [28]. It is a complex nonlinear process which can exponentially amplify a small disturbance, leading to a drastic change in the system, such as the optical rogue-wave formation in fibers. Despite the strong interest, characteristics of optical rogue waves are not yet fully understood. One prime example of such an unresolved scenario is the process of continuous-wave supercontinuum generation (CW-SCG), where MI plays a pivotal role [29]. Here, the pump can be considered as a higher-order soliton with a very large soliton number [30]. The evolution is then

dominated by a noise-seeded MI, leading to its breakup [31]. The disintegration is highly nontrivial and is a multistage process. At the beginning of the evolution, the presence of noise among the large number of solitons makes the higher-order soliton unstable, leading to its collapse. Immediately before the collapse, a wide variety of rogue-wave-type substructures appear. In the final stage, all the substructures become a collection of fundamental solitons. The physics behind the creation of a large number of solitons from the CW is not very well studied.

The NLSE permits fundamental and higher-order rogue-wave solutions [32]. In its normalized form, the fundamental rogue wave has the maximum amplitude of 3, while a higher-order rogue wave of order  $N$  consists of  $N(N+1)/2$  fundamental rogue waves and reaches the maximum amplitude of  $2N+1$ . They can be excited numerically via noise-driven MI [33].

In this work, using the generalized nonlinear Schrödinger equation (GNLSE), we show that, when the NLSE is perturbed with the third-order dispersion (TOD), self-steepening (SS), and Raman-induced self-frequency shift (RIFS) effects, a higher-order rogue-wave solution undergoes fission, similar to the higher-order soliton fission. We take each effect individually as well as simultaneously in our analysis. An investigation of the fission under TOD is already comprehensively described in Ref. [34]. Hence, in the current monograph, we only focus on the SS and RIFS effects to show that each of these also breaks the higher-order rogue wave to its constituent parts. Furthermore, using a local inverse-scattering technique (IST) [35–37] based on a periodized local structure, we demonstrate that the rogue-wave solution under the influence of RIFS effect generates various other local substructures such as solitons and breathers in the neighborhood. As we shall see, while all these effects induce a rogue-wave

fission, it is the RIFS effect that has the major impact on transforming the disintegrated rogue wave to solitons. Finally, we solve the full GNLS numerically to study the combined effect of the TOD, SS, and RIFS on the rogue-wave fission, as well as its long-time evolution.

The article is organized as follows. In Secs. III and IV, we investigate the effect of SS and RIFS on a second- and third-order rogue waves, revealing that each of them individually induces a rogue-wave fission. We also demonstrate that under the RIFS effect, higher-order rogue waves generate red-shifted frequency components while decelerating, until eventually transforming into a soliton. In Sec. V, we examine the combined influence of the TOD, SS, and RIFS effects, showing that after the fission, the evolving rogue-wave components create asymmetrical spectral profiles with both red- and blue-shifted frequencies.

## II. MODEL, SOLUTIONS, AND TECHNIQUES

The GNLS in its normalized form is

$$\begin{aligned} i \frac{\partial \psi}{\partial z} - \frac{\beta_2}{2} \frac{\partial^2 \psi}{\partial t^2} + \gamma \psi |\psi|^2 \\ = i \epsilon_3 \frac{\partial^3 \psi}{\partial t^3} - i s \frac{\partial}{\partial t} (\psi |\psi|^2) + \tau_R \psi \frac{\partial |\psi|^2}{\partial t}, \end{aligned} \quad (1)$$

where  $\psi = \psi(z, t)$  is the complex field envelope, and  $z$  and  $t$  are the evolution and transverse variables, respectively.  $\epsilon_3$  is the TOD parameter, and  $s$  and  $\tau_R$  are the coefficients of SS and RIFS, with their explicit expression given by

$$\epsilon_3 = \frac{\beta_3}{6|\beta_2|t_0}, \quad s = \frac{1}{\omega_0 t_0}, \quad \tau_R = \frac{T_r}{t_0}, \quad (2)$$

where  $\beta_2$  is the group velocity dispersion,  $\gamma$  is the nonlinear strength,  $\beta_3$  is the coefficient of TOD,  $\omega_0$  is the carrier angular frequency,  $t_0$  is the pulse duration, and  $T_r$  is the Raman time constant [38]. Since the coefficients of TOD, SS, and RIFS in Eq. (1) are inversely proportional to the pulse duration  $t_0$ , they are negligible in the long pulse regime, while they contribute significantly in the ultrashort pulse regime.

With the group-velocity dispersion parameter  $\beta_2 = -1$ , nonlinear parameter  $\gamma = 1$ , and  $\epsilon_3 = s = \tau_R = 0$ , Eq. (1) is the NLSE and is the most basic equation that can be used to model optical pulse propagation in nonlinear dispersive media [39]. This form of the equation can be solved analytically using the inverse scattering transformation [40,41]. Equation (1) with specific ratios of TOD, SS, and RIFS effect can become integrable, permitting rogue-wave solutions [42]. In this work, however, we assume that the TOD, SS, and RIFS effects are arbitrary and solve Eq. (1) numerically.

To numerically generate higher-order rogue waves, we adopt the analytic solutions of the NLSE as the initial conditions well before their fully developed stage. Specifically, we use the second- and third-order rogue-wave solutions as presented in Ref. [32] [see Eqs. (23) and (26)]. The solutions in their exact forms can be obtained by solving the NLSE through Darboux transformation technique using a continuous wave,  $\psi = \exp(iz)$ , as the seed [43]. The details of the numerical technique employed to excite higher-order rogue waves can be found in Ref. [34]. We should mention that by

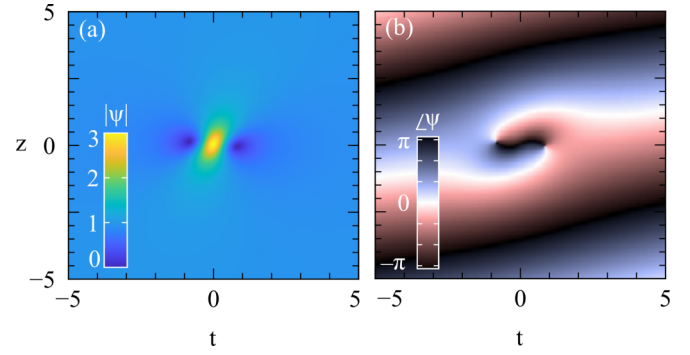


FIG. 1. (a) Amplitude and (b) phase profiles of the rogue wave from Eq. (4) with  $s = 0.2$ . It has the maximum amplitude of 3 with a distorted phase shift of  $\pi$  across the peak. Note that this solution is formed at  $t = z = 0$  because of the closed-form nature of the analytic solution.

applying different initial conditions, various other breather-like solutions can be numerically excited [29,44].

We also study the impact of higher-order rogue-wave fission on the surrounding wave background under the influence of RIFS effect. A variety of waves emerge in the neighborhood of the rogue wave that undergoes fission. We employed a local IST to identify the types of waves that are formed. The details of the technique and its implementation are outlined in Refs. [35–37].

## III. EFFECT OF SELF-STEEPENING

Including the SS effect on the NLSE, the equation becomes

$$i \frac{\partial \psi}{\partial z} - \frac{\beta_2}{2} \frac{\partial^2 \psi}{\partial t^2} + \gamma \psi |\psi|^2 + i s \frac{\partial}{\partial t} (\psi |\psi|^2) = 0 \quad (3)$$

where  $s$  is the coefficient of the SS effect. The first-order rogue-wave solution of Eq. (3) can be extracted from the rogue-wave solution of a cubic-quintic NLSE presented in Ref. [45]. After reformulating it into a simpler form, it is given as

$$\psi_s(z, t) = \left( 1 - \frac{G + iHz + 8i\tau}{D_s} \right) e^{i[z(1+\frac{1}{2}s^2) - t\tau + \Phi]}, \quad (4)$$

where  $\tau = t - zs$ ,  $\kappa = 1 + s^2$  and

$$D_s = D + 4is(2\tau - t) + 4s\tau(s\tau - 2z),$$

$$D = 1 + 4t^2 + 4z^2,$$

$$\Phi = 2 \tan^{-1} \left[ \frac{4s(zs - \tau)}{1 + 4\kappa(z^2 + \tau^2)} \right].$$

With  $s \rightarrow 0$  it directly reduces to fundamental rogue-wave solution [4]. The SS effect induces a drift velocity [46], proportional to  $s$ , in the development of the rogue wave along with a distorted time-varying phase profile presented in Figs. 1(a) and 1(b), respectively. The SS effect induced velocity also makes the rogue wave to appear tilted at its emerging point [47].

Note that with  $s = 0$ , the phase profile of a fundamental rogue wave  $\psi(t, z = 0)$  across the maximum amplitude at  $z = 0$  remains flat with a  $\pi$  phase shift as seen in Fig. 2(b). A finite

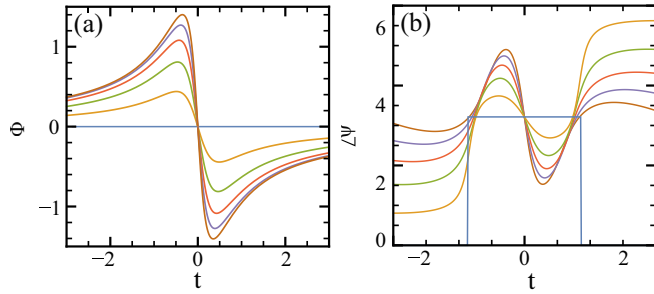


FIG. 2. (a) The phase term  $\Phi$ . (b) Total phase profiles of the rogue wave from Eq. (4). The coefficient  $s$  is varied from 0 to 1. The light-blue lines are when  $s = 0$ .

SS effect deforms the phase profile for a range of  $s$  values. While that modification is the result of several contributions, we highlight that the deformation around  $t = 0$  is mostly due to the pure phase term  $\Phi$  in Eq. (4). In Fig. 2(a), we present the dependence of  $\Phi$  on  $t$  for a varying  $s$  from 0 to 1. We shall see later that the  $\Phi$  phase term is responsible for a sharp spectral dip in the frequency profile of the rogue wave.

### A. Second-order rogue-wave fission

Taking the exact analytic NLSE second-order rogue-wave solution as the initial condition, we numerically solved Eq. (3) for a range of  $s$  values. We find that in the presence of SS, the second-order rogue wave experiences fission, breaking apart the structure shown in Fig. 3(a) and its phase in Fig. 3(b) into three fundamental rogue waves. We observe that the disintegrated first-order components display the same temporal and phase characteristics as those in Fig. 1. Most importantly, we observe that the SS effect also shifts the disintegrated rogue waves in the  $t$  direction.

When  $s = 0$ , the growth of MI for each of these fundamental rogue waves is the same, resulting in the bound state formation of a second-order rogue wave. However, the SS effect breaks this degeneracy, allowing a space-time-varying MI development among the individual rogue waves. Each of the breakaway rogue waves experiences different translational distance in the positive  $t$  direction, inhibiting the bound state, and leading to three fundamental rogue waves each appearing in a distinct position and time. Note that with a weak perturbation ( $s = 0.04$ ), the transient fission state with three fundamental rogue waves linked together are marked within the dashed white box in Figs. 3(c) and 3(d). Within this box, a doublet with two conjoined first-order rogue waves formed in the right side while the other is on the left. With a stronger  $s$ , separation distance among the disintegrated rogue waves increases as shown in the temporal evolutions in Figs. 3(e) and 3(g) with changing phase profiles as evident in Figs. 3(f) and 3(h). The modulated phase profile of each of the separated rogue waves closely matches that of the first-order rogue wave shown in Fig. 1(b).

### B. Third-order rogue-wave fission

The effect of SS on a third-order rogue wave shown in Figs. 4(a) and 4(b) is similar to that on the second-order one. To observe its fission under the influence of nonzero

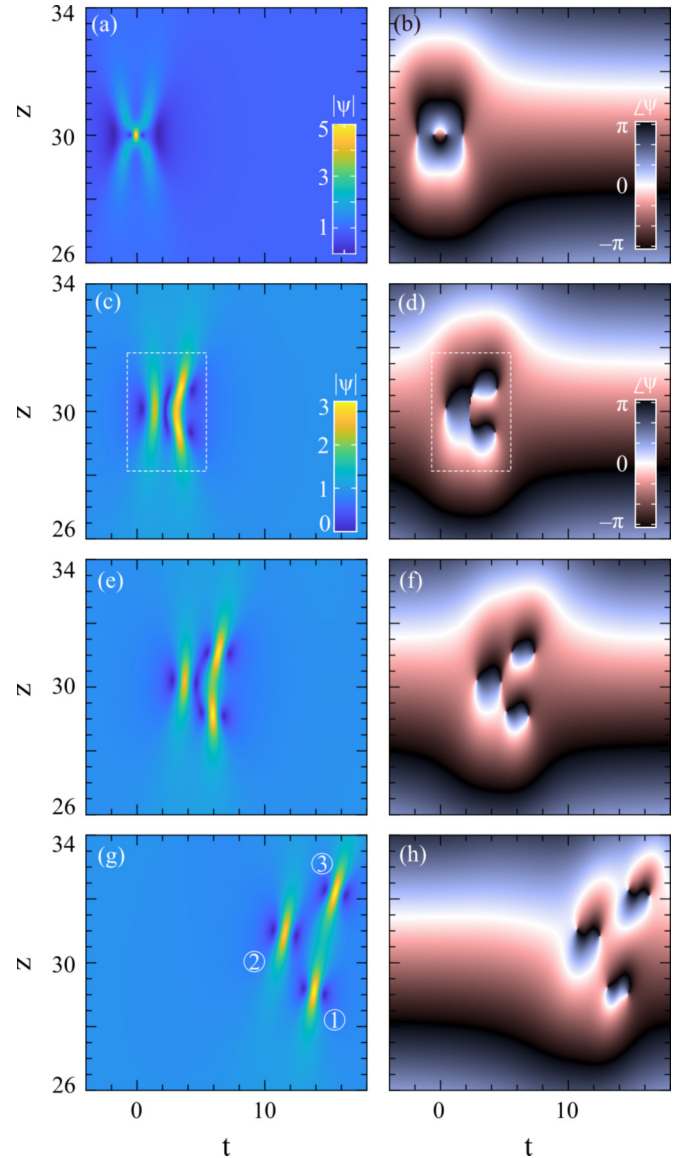


FIG. 3. A second-order rogue wave under the influence of SS effect. Temporal and phase profiles when (a, b)  $s = 0.0$ , (c, d)  $s = 0.04$ , (e, f)  $s = 0.08$ , and (g, h)  $s = 0.2$ .

$s$ , we plot a few examples. When  $s = 0.04$ , the onset of a second-order rogue wave within the white-dotted box is clear, along with a group of three underdeveloped first-order rogue waves to its right. This is observable in Figs. 4(c) and 4(d). The emerging point is slightly translated towards the positive  $t$ . When  $s = 0.06$ , the fission produces a triplet within the white-dotted box instead of a second-order rogue wave. The triplet corresponds to a transient state of three conjoined first-order rogue waves. Note that there is another group of three first-order rogue waves to its right. These are tied to the three underdeveloped rogue waves that appear to the right-hand side of the white-dotted box in Figs. 4(c) and 4(d).

When  $s$  is stronger, at 0.2, the third-order rogue wave completely breaks apart into six fundamental rogue waves. This is shown in Figs. 4(g) and 4(h). They are well separated and arranged in an asymmetric way, located at transversely shifted positions. Rogue waves 2, 3, and 5 are linked to the

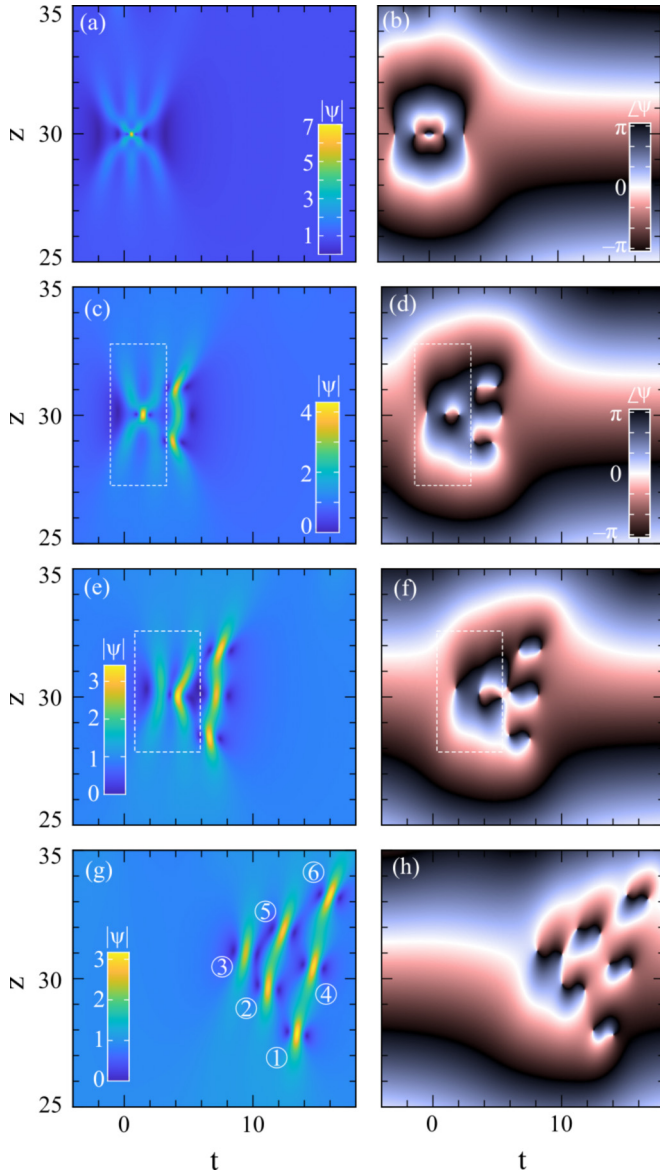


FIG. 4. Temporal and phase profiles of a third-order rogue wave when (a), (b)  $s = 0$ , (c), (d)  $s = 0.01$ , (e), (f)  $s = 0.06$ , and (g), (h)  $s = 0.2$ .

second-order rogue wave and triplet in Figs. 4(c) and 4(d) and Figs. 4(e) and 4(f), respectively, whereas rogue waves 1, 4, and 6 correspond to the three first-order rogue waves that disintegrate at smaller  $s$  values beside the second-order rogue wave or triplet. The appearance of a second-order rogue wave as shown in Figs. 4(c) and 4(d) at a small value  $s$  indicates that under a weak perturbation, the higher-order rogue wave disintegrates only partially, revealing its underlying composite pattern. A comparatively strong perturbation is required to achieve a complete disintegration.

### C. Spectrum

The time-varying phase in each of the fissioned rogue waves developed during the evolution under the SS effect results in a sharp asymmetrical spectral broadening. To understand the spectral behavior, we study the exact solution of

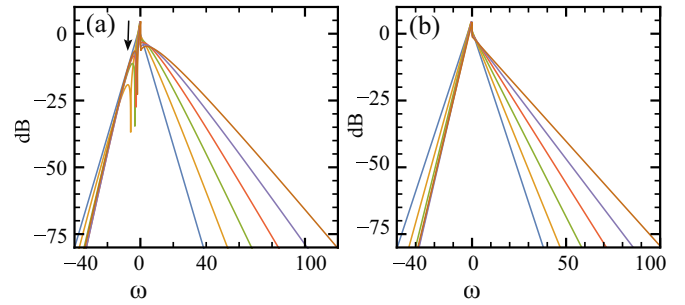


FIG. 5. Spectra at  $\psi(z = 0, t)$  (a) with a finite  $\Phi$  and (b) with  $\Phi = 0$  when  $s$  is varied from 0 to 1. A cusp develops in all cases for nonzero  $\Phi$  except when  $s = 0$ .

a first-order rogue wave by taking the Fourier transformation of Eq. (4) at  $z = 0$ . For a fundamental rogue wave with  $s = 0$ , the spectrum is

$$F(\omega, s = 0, z = 0) = \sqrt{2\pi} \left[ -e^{-\frac{|\omega|}{2}} + \delta(\omega) \right], \quad (5)$$

where  $\delta$  is the Dirac delta.

For  $s \neq 0$ , the expression becomes

$$F(\omega, s, z = 0) = \sqrt{2\pi} \delta(\omega - s) - \left\{ a(s) e^{b(s)(\omega - s)} \left( \omega + \frac{1}{s} \right) [c(s)\theta(s - \omega) e^{d(s)(\omega - s)} + f(s)\theta(\omega - s)] \right\}, \quad (6)$$

where  $a(s)$ ,  $b(s)$ ,  $c(s)$ ,  $d(s)$ , and  $f(s)$  are numerical coefficients that are not so crucial, while  $\theta$  is the Heaviside step function. One can observe that, due to the first factor on the second line of Eq. (6), the Fourier transform becomes exactly 0 for  $\omega = -1/s$ .

We plot several spectral profiles in Fig. 5(a) with  $s$  varying from 0 to 1. For  $s = 0$ , the innermost triangular NLSE spectral profile is symmetric around  $\omega = 0$ . However, when  $s \neq 0$ , the spectral profiles become broadened and increasingly asymmetric. Interestingly, a cusp appears in each of the profiles, which is indicated by a black arrow in Fig. 5(a), at  $\omega = -1/s$ . If we artificially set the term  $\Phi$  in Eq. (4) to be 0, the spectrum remains mostly unchanged but the cusp disappears. This indicates that the time-varying nonlinear phase development shown in Fig. 2(a) plays a key role in the spectral dynamics with the SS effect.

These spectral features also arise in the numerical simulations of SS-induced fission dynamics of higher-order rogue waves. In Fig. 6(a) three distinct asymmetrical spectra 1, 2, and 3 correspond to the three number-labeled rogue waves formed in Figs. 3(g) and 3(h). Similarly, the spectra in Fig. 6(b) correspond to the six disintegrated rogue waves presented in Figs. 4(g) and 4(h). While in Figs. 4(g) and 4(h) the spectral features of rogue waves 1 and 6 appear undisturbed, those from rogue waves 2–5 are mutually interacting, giving rise to an interference pattern. Note that the same spectral cusp which we have observed in the analytic first-order rogue wave also arises in the higher-order cases and it is marked with white arrows in Fig. 6.

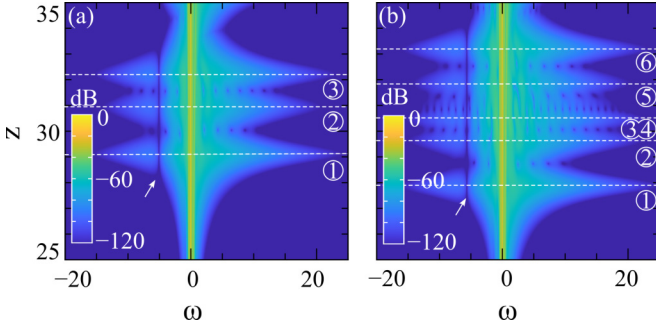


FIG. 6. (a), (b) Spectral profiles of the evolutions presented in Figs. 3(g) and 3(h) and Figs. 4(g) and 4(h), respectively, with  $s = 0.2$ . The number labels indicate the corresponding first-order rogue waves in Figs. 3(g), 3(h), 4(g), and 4(h).

IV. EFFECT OF RIFS

The study of Raman effect on rogue waves has so far been done mostly on the first-order rogue wave [48–50] and breather solutions [51]. Similar studies on higher-order rogue waves have not been reported until now. To include the RIFS effect, we use the equation

$$i \frac{\partial \psi}{\partial z} - \frac{\beta_2}{2} \frac{\partial^2 \psi}{\partial t^2} + \gamma \psi |\psi|^2 - \tau_R \psi \frac{\partial |\psi|^2}{\partial t} = 0, \quad (7)$$

The RIFS effect in Eq. (7) is a non-Hamiltonian term, and hence the equation does not exhibit an analytic solution. This means that the energy of the evolving rogue wave structure is not preserved [52]. As a result, when the rogue wave is evolving in  $z$ , it dissipates energy, altering its amplitude and width while the central frequency red-shifts.

Under a weak RIFS effect, the disintegration of higher-order rogue wave follows similar steps as for the SS effect. For instance, when we apply  $\tau_R = 0.008$  on a second-order rogue wave and observe its fission, it breaks down into a doublet (two first-order rogue waves joined together) to the left and a first-order rogue wave to the right at around  $z = 30$  and  $t = 0$ , as shown in Fig. 7(a). The separated first-order rogue wave immediately assumes the flight trajectory of a soliton and gradually slows down. Along the path, while it decelerates in the positive  $t$  direction, it emits red-shifted frequency radiations as can be seen in Fig. 7(b). The energy dissipation continues, forming a bent trajectory in the temporal domain. Similar behaviors are noted for a third-order rogue-wave fission in Figs. 7(c) and 7(d). As a result of the noise-driven MI, a breather-type structure forms at  $z \approx 40$ , creating discrete spectral components (a striped pattern) around  $\omega = 0$ .

A complete disintegration of higher-order rogue waves requires a stronger  $\tau_R$  value. Figure 8(a) demonstrates a disintegration of a second-order rogue wave into three fundamental rogue waves when  $\tau_R = 0.25$ . With such a strong RIFS effect, the separated rogue waves are distorted significantly. A similar observation is also noted in the case of a third-order rogue wave for the same value of  $\tau_R$  as shown in Fig. 8(b). The third-order rogue wave fissions into six heavily distorted fundamental rogue waves.

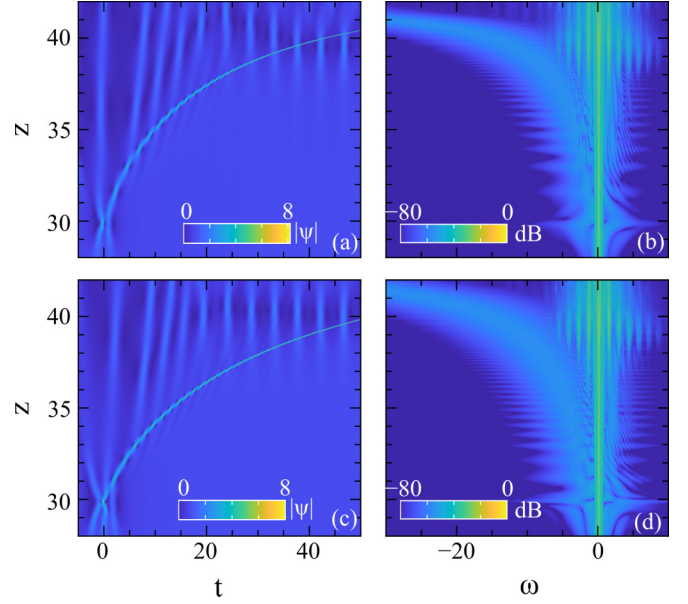


FIG. 7. Impact of RIFS in (a) temporal and (b) spectral domains for a second-order rogue wave with  $\tau_R = 0.008$ , and (c) temporal and (d) spectral domains for a third-order rogue wave with  $\tau_R = 0.005$ .

A. Long-time evolution under RIFS effect and its impact on the background

When a higher-order rogue wave emerges under the influence of RIFS effect, it significantly changes the neighboring background wave, revealing rich dynamical features. This is demonstrated in Fig. 9, where we simulate a second-order rogue wave with  $\tau_R = 0.004$  for an extended propagation length  $z$  of up to 50. The continuous-wave background is now highly distorted, with a variety of other waves appearing in the neighborhood. To classify the types of waves formed, we take the solution at  $z = 43.8$ , indicated by a white dashed line in the top panel in Fig. 9. The corresponding amplitude is plotted in the middle panel. We select six representative profiles (within shadows) from the solution at  $z = 43.8$  and periodize each of them hundreds of times to employ the local-IST spectral analysis. This reveals their corresponding local-IST spectra, from which we can identify the types of waves formed around the emerging rogue wave [35]. The local-IST procedure on the shaded localized structures reveals a combination

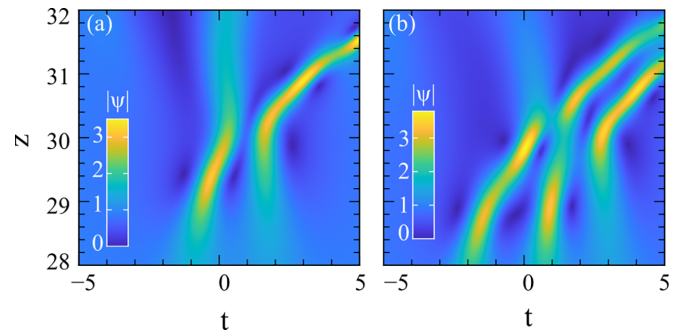


FIG. 8. Fission of (a) a second-order and (b) a third-order rogue wave under the influence of a strong RIFS effect with  $\tau_R = 0.25$ .

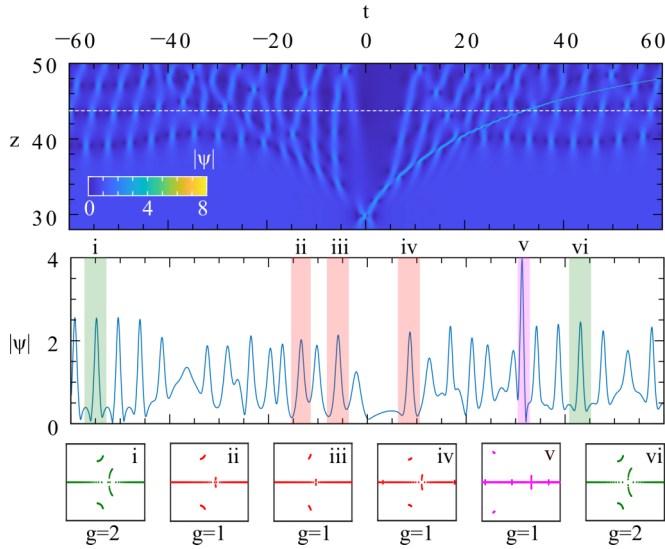


FIG. 9. (Top) Long-time evolution of a second-order rogue wave under the influence of RIFS effect with  $\tau_R = 0.004$ . (Middle) Amplitude extracted at  $z = 43.8$  corresponding to the white dashed line in the top panel. (Bottom) Local-IST spectra of the structures under the shaded areas in the middle panel.

of IST bands. They are shown in the bottom panel in Fig. 9. The classification is such that, if the number of bands is  $m$ , the genus  $g$  of the structure is  $m - 1$ . The structures within the green-shaded areas, i.e., (i) and (vi), have three spectral bands, making them  $g = 2$ -type solutions, which are associated with either breathers or rogue waves [37]. Similarly, (ii), (iii), and (iv) in the pink-shaded areas exhibit two IST bands, belonging to  $g = 1$ -type solutions and classified as solitons.

In the magenta-shaded area, a soliton is created from the decelerating rogue wave. The corresponding eigenvalues shown in (v) in the bottom panel is not centered around the real line. This occurs because the shape of the soliton is highly asymmetric. These observations indicate that higher-order rogue waves under the influence of RIFS effect trigger the formation of a series of other waves around it, such as breathers and solitons.

Note that MI remains active in the wave field from the beginning of the evolution. While the rogue wave is taking its shape, the background instability seeded by noise also undergoes amplification. The appearance of rogue waves at  $z = 30$  reinforces the background MI to reach the first growth-return cycle at  $z \approx 40$ , and subsequent breather-type formation takes place thereafter.

## V. COMBINED EFFECT

We now address the case where all three perturbations—TOD, SS, and RIFS effects—are present. We find that the process of rogue-wave fission persists. Figure 10(a) is the temporal evolution of a second-order rogue-wave fission. We observe that all the disintegrated components assume the same trajectory towards the positive  $t$  direction. When a higher-order rogue wave fissions, the individual components appear in a triangular arrangement in the  $t$ - $z$  plane. For instance, in

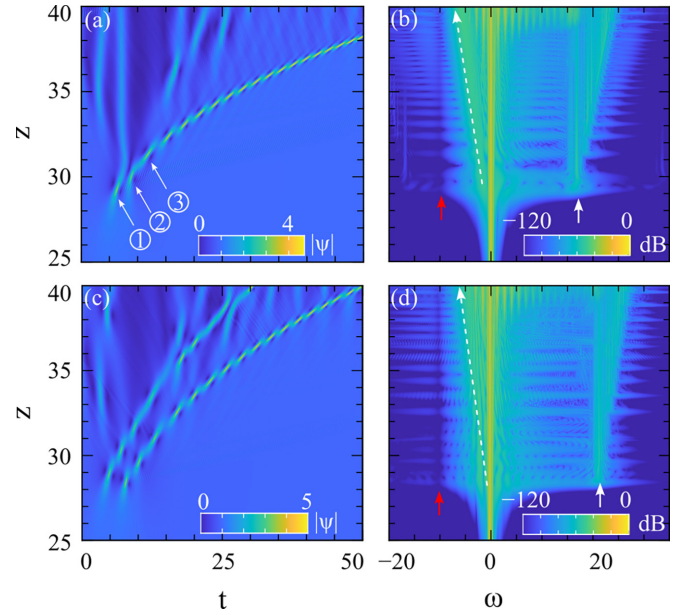


FIG. 10. Combined effect of TOD, SS, and RIFS on higher-order rogue waves. (a), (b) Temporal and spectral evolutions of a second-order rogue wave with  $\epsilon_3 = 0.2$ ,  $s = 0.10$ , and  $\tau_R = 0.008$ . (c), (d) Temporal and spectral evolutions of a third-order rogue wave with  $\epsilon_3 = 0.15$ ,  $s = 0.10$ , and  $\tau_R = 0.005$ .

Fig. 3(g), rogue waves 1, 2, and 3 form a triangle. A similar arrangement also appears for fission under the TOD effect, except that rogue waves 1 and 3 develop in the opposite side of 2. See Fig. 3 in Ref. [34]. When TOD and SS effects act simultaneously, these opposite features cancel each other out, aligning them in  $t$ . Since the RIFS effect is inversely proportional to the pulse duration  $t_0$ , the rogue-wave duration must be short enough to come under the active influence of RIFS effect. In Fig. 10(a), which shows the temporal evolution of a second-order rogue wave with  $\epsilon_3 = 0.2$ ,  $s = 0.10$ , and  $\tau_R = 0.008$ , rogue waves 1 and 2 remain stationary because their durations are too long to be affected by RIFS. However, rogue wave 3 is at the trailing position and achieves comparatively shorter duration that places it under the influence of RIFS, resulting in a bent trajectory. For a more solid understanding, an analytic treatment of this problem is essential. This will be addressed in our future work.

The dynamics become more clear in the spectral domain as shown in Fig. 10(b). Rogue waves 1 and 2 do not generate red-shifted frequency components. Nevertheless, due to the presence of TOD, they generate dispersive waves indicated by the white arrow. On the contrary, rogue wave 3 undergoes RIFS and continues to lose energy along the propagation. The repeated compression stages of rogue wave 3 create a cascaded emission of dispersive wave. A steady red-shifting is clearly visible within the frequency range  $\omega = 0$  to  $-10$ , as indicated by the white dashed arrow in Fig. 10(b). As discussed earlier, a spectral cusp marked by the red arrow appears due to the SS effect. The combined effect applied on a third-order rogue wave follows similar dynamical features as shown in Figs. 10(c) and 10(d).

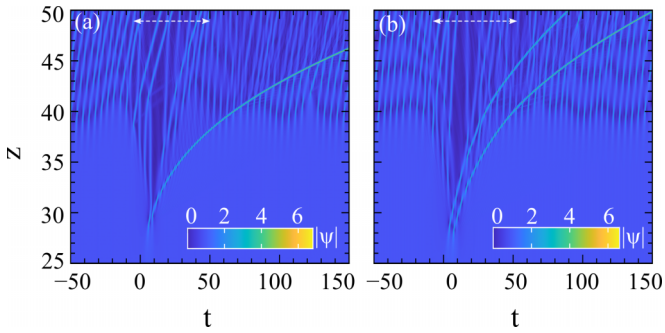


FIG. 11. Long-time evolutions of (a) Fig. 10(a) and (b) Fig. 10(c).

### A. Long-time evolution under combined effects

As the system keeps evolving, the disintegrated rogue waves eventually transform into a collection of fundamental solitons. This is shown in Figs. 11(a) and 11(b), which are the extended evolutions of Figs. 10(a) and 10(c), respectively. The fission triggers a group of comparably low-amplitude and straight-moving solitons around the central region, indicated by the white dashed horizontal arrow. However, out of these components broken out from the second-order rogue wave, one transforms into a high-amplitude soliton that proceeds in a bent trajectory. For a third-order rogue wave, two of the broken parts become the high-amplitude solitons. In both cases, a breather-type formation emerges on the sides of the evolution field due to MI. We note that the trajectories of low-amplitude solitons around the central region are only weakly bent. Their durations are not short enough to be influenced significantly by the RIFS effect.

### B. Demonstration in a long-pulse supercontinuum generation

The rogue-wave formation, its fission, and their subsequent transformation to solitons can be observed in MI-induced SCG. A long launch pulse corresponding to a higher-order soliton of very large soliton number undergoes the MI and the end product is hundreds of solitons [53,54]. We demonstrate this numerically by simulating the propagation of  $N = 300$  solitons in Eq. (1) with the combined effect of TOD, SS, and RIFS. The evolution dynamics in the temporal domain is presented in Fig. 12(a). It shows that the noise-driven MI leads to the formation of rogue-wave-type substructures and eventually transforms into many solitons. The onset of MI is clearly visible in the spectral domain in Fig. 12(b) with the appearance of two side lobes, indicated by the two white arrows around  $\omega = 0$ . The red arrow shows the discontinuity in the spectral contents due to the SS effect.

A plane-wave background can be considered as an ensemble of an infinite number of solitons [30,55]. Noise among the solitons can spontaneously trigger MI, which leads to the development of both fundamental as well as higher-order rogue waves [33]. If the formation is a fundamental rogue wave, the concurrent influence of TOD, SS, and RIFS transforms it directly into a small number of those solitons [56]. However, in the same scenario, if MI contributes to form a higher-order rogue wave, it initially disintegrates into a group of fundamental rogue waves, which then in the later stage transform into a bunch of solitons as shown in Fig. 12(a). A magnified

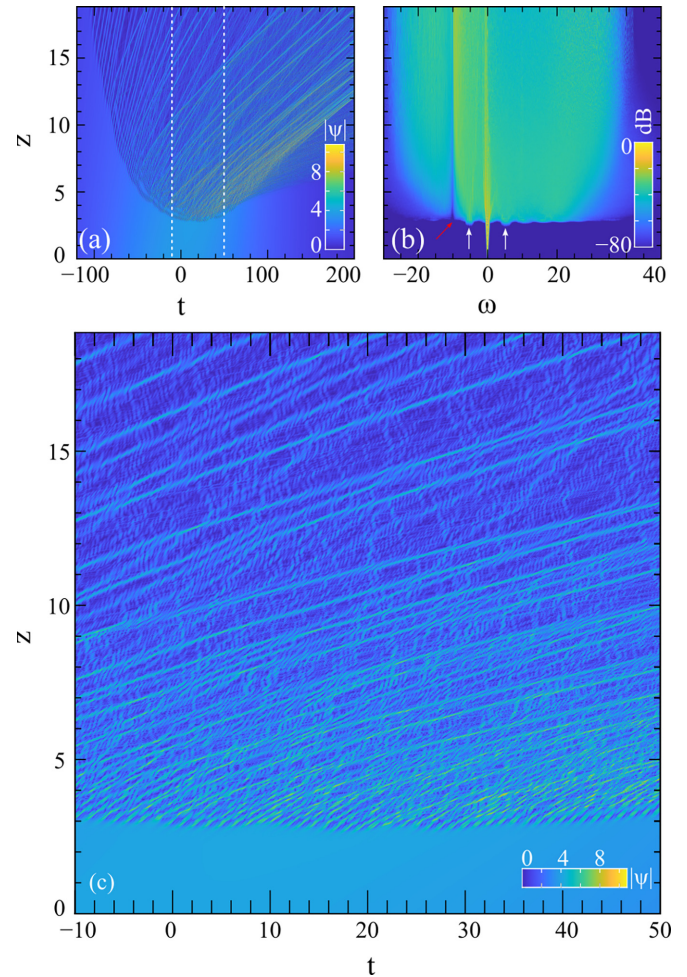


FIG. 12. (a) Temporal and (b) spectral evolutions of a  $N = 300$  soliton when  $s = 0.1$ ,  $\epsilon_3 = 0.03$ , and  $\tau_R = 0.001$ . (c) A magnified plot around the central region indicated by the two parallel white dotted lines where the breather-type structure transforms to many solitons.

plot of these transformations are shown in Fig. 12(c). In fact, this multistep process of transformation is not quite apparent in Figs. 12(a) or 12(c). This is because the applied perturbations are too strong to observe the delicate nature of the higher-order rogue-wave fission procedure and their successive transformation to solitons. The disintegrated higher-order rogue waves are highly distorted and already in a state of soliton formation, making the observation of individual steps difficult. From Fig. 12(c), we can only say that whether it is a fundamental rogue wave or a higher-order rogue wave that forms in the initial stage, the end product of the combined effects is always a large collection of fundamental solitons.

In an effort to capture a clear higher-order rogue-wave fission and its transformation steps to solitons in a MI-induced SCG, we solve the system with the identical initial condition, i.e.,  $N = 300$ , but with very weak perturbations of  $s = 0.02$ ,  $\epsilon_3 = 0.002$ , and  $\tau_R = 0.0001$ . This is shown in Fig. 13(a) with an initial evolution distance of  $z = 2\pi$ . For reference, the evolution in a system without the perturbations is presented in Fig. 13(b) for the same initial condition, including the seeded

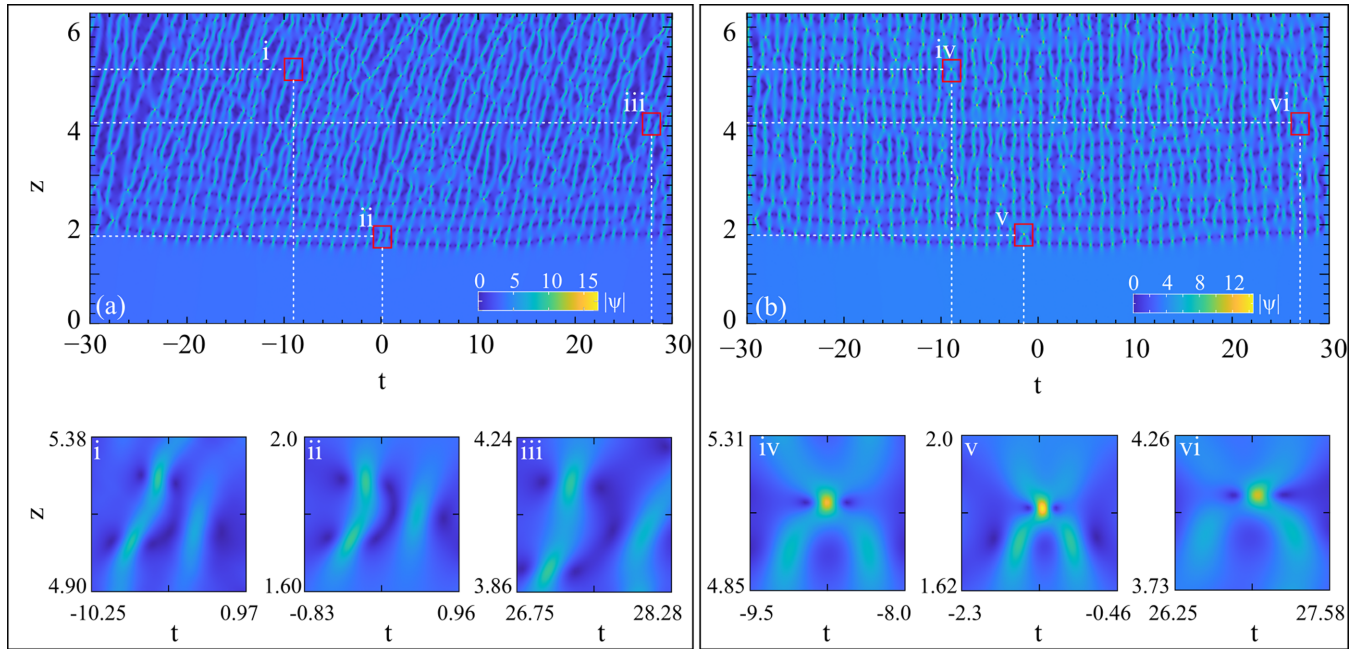


FIG. 13. Evolution of a higher-order soliton of  $N = 300$  when (a)  $s = 0.02$ ,  $\epsilon_3 = 0.002$ , and  $\tau_R = 0.0001$ , and (b) in the absence of the higher-order effects. (iv), (v), and (vi) in (b) are the instances of second-order rogue waves in the unperturbed system. The corresponding second-order rogue-wave fissions are shown in (i), (ii), and (iii).

noise. In the latter, breather-type formations appear with no transverse velocity. They make frequent collisions, leading to higher-order rogue-wave formations. A collision between two breathers creates a second-order rogue wave around the collision point, a collision among three creates a third-order rogue wave, and so on. Note that the higher-order rogue waves can also appear independently without the collision. Several instances of second-order rogue waves are isolated in Fig. 13(b) as (iv), (v), and (vi) within the red boxes. Corresponding enlarged views of them are presented at the bottom. We should mention that, due to the nonideal initial condition, the amplitudes of the formed second-order rogue waves are not exactly 5 as in the ideal case.

The isolated second-order rogue waves in Fig. 13(b) appear disintegrated in the presence of the weak perturbations as (i), (ii), and (iii) in Fig. 13(a). Their magnified views clearly indicate that each of the second-order rogue waves breaks apart into three fundamental rogue waves. The white dotted lines are marking the exact locations of the second-order rogue-wave formations and their corresponding fission positions. Note that due to the SS effect, the fission positions are slightly shifted in the positive  $t$  direction.

## VI. CONCLUSION

We showed that a higher-order rogue wave can undergo fission in a system weakly perturbed by SS and RIFS. Employing the second- and third-order rogue-wave solutions in the presence of these effects, we revealed their breaking mechanisms. In the weakly perturbed regime, the higher-order rogue wave first partially disintegrates, revealing its hierarchical pattern. For instance, the second-order rogue wave exhibits

one doublet and a first-order rogue wave. Similarly, the third-order rogue wave exposed that it is built on a second-order rogue wave and three separate fundamental rogue waves. As the perturbations become stronger, the higher-order rogue waves undergo the intermediary process of rogue-wave fission into their constituent fundamental rogue waves, then eventually into solitons. Also, we demonstrate that since RIFS is a dissipative term, the disintegrated rogue wave loses energy and decelerates during its evolution, which appears as a red shift in the frequency domain. It eventually transforms the rogue wave into one or more high-amplitude fundamental solitons.

With the simultaneous influence of TOD, SS, and RIFS, we observed that the higher-order rogue waves trigger a collection of solitons on the background after the fission. This is a multistep process and the fission of higher-order rogue waves can only be observed when they are under the influence of weak perturbations. In the frequency domain this rogue-wave-to-soliton transformation appears as blue- and red-shifted spectral components with an asymmetric profile. These observations provide insights into the process of MI, which can be beneficial for interpreting various nonlinear phenomena in optics, hydrodynamics, and other similar systems.

This study is a step forward in demonstrating how major fiber optical effects can influence the evolution of higher-order rogue waves. There are still many open questions that need to be answered. For example, we do not know why from multiple disintegrated rogue waves, only one or two rogue waves are taking the path to become the high-amplitude fundamental solitons. An analytical approach is likely required to address this question. Moreover, we understand that the application

of the local-IST procedure to identify solitons, breathers, and rogue waves in a chaotic wave field as we employed here is still a developing research area. We believe our work in this manuscript will stimulate more studies and discussions in this direction.

## ACKNOWLEDGMENTS

A.C. and M.B. acknowledge Nanyang Technological University, NAP-SUG grant. W.C. acknowledges funding support from the Ministry of Education–Singapore, AcRF Tier 1 RG135/20.

- 
- [1] N. Akhmediev, A. Ankiewicz, and M. Taki, Waves that appear from nowhere and disappear without a trace, *Phys. Lett. A* **373**, 675 (2009).
- [2] M. Onorato, A. R. Osborne, M. Serio, and S. Bertone, Freak Waves in Random Oceanic Sea States, *Phys. Rev. Lett.* **86**, 5831 (2001).
- [3] P. Müller, C. Garrett, and A. Osborne, Rogue waves, *Oceanography* **18**, 66 (2005).
- [4] B. Kibler, J. Fatome, C. Finot, G. Millot, F. Dias, G. Genty, N. Akhmediev, and J. M. Dudley, The Peregrine soliton in nonlinear fibre optics, *Nat. Phys.* **6**, 790 (2010).
- [5] W. Moslem, P. Shukla, and B. Eliasson, Surface plasma rogue waves, *Europhys. Lett.* **96**, 25002 (2011).
- [6] L. Stenflo and M. Marklund, Rogue waves in the atmosphere, *J. Plasma Phys.* **76**, 293 (2010).
- [7] V. B. Efimov, A. N. Ganshin, G. V. Kolmakov, P. V. E. McClintock, and L. P. Mezhov-Deglin, Rogue waves in superfluid helium, *Eur. Phys. J. Spec. Top.* **185**, 181 (2010).
- [8] Y. V. Bludov, V. V. Konotop, and N. Akhmediev, Vector rogue waves in binary mixtures of Bose-Einstein condensates, *Eur. Phys. J.: Spec. Top.* **185**, 169 (2010).
- [9] M. Shats, H. Punzmann, and H. Xia, Capillary Rogue Waves, *Phys. Rev. Lett.* **104**, 104503 (2010).
- [10] G. Veldes, J. Borhanian, M. McKerr, V. Saxena, D. Frantzeskakis, and I. Kourakis, Electromagnetic rogue waves in beam–plasma interactions, *J. Opt.* **15**, 064003 (2013).
- [11] W. Moslem, R. Sabry, S. E.-Labany, and P. Shukla, Dust-acoustic rogue waves in a nonextensive plasma, *Phys. Rev. E* **84**, 066402 (2011).
- [12] Y.-Y. Tsai, J.-Y. Tsai, and I. Lin, Generation of acoustic rogue waves in dusty plasmas through three-dimensional particle focusing by distorted waveforms, *Nat. Phys.* **12**, 573 (2016).
- [13] Y. V. Bludov, V. V. Konotop, and N. Akhmediev, Matter rogue waves, *Phys. Rev. A* **80**, 033610 (2009).
- [14] B. Kibler, K. Hammani, C. Michel, C. Finot, and A. Picozzi, Rogue waves, rational solitons and wave turbulence theory, *Phys. Lett. A* **375**, 3149 (2011).
- [15] Y. Zhen-Ya, Financial rogue waves, *Commun. Theor. Phys.* **54**, 947 (2010).
- [16] D. R. Solli, C. Ropers, P. Koonath, and B. Jalali, Optical rogue waves, *Nature (London)* **450**, 1054 (2007).
- [17] A. Montina, U. Bortolozzo, S. Residori, and F. T. Arecchi, Non-Gaussian Statistics and Extreme Waves in a Nonlinear Optical Cavity, *Phys. Rev. Lett.* **103**, 173901 (2009).
- [18] S. Residori, U. Bortolozzo, A. Montina, F. Lenzini, and F. Arecchi, Rogue waves in spatially extended optical systems, *Fluct. Noise Lett.* **11**, 1240014 (2012).
- [19] C. Lecaplain, P. Grelu, J. Soto-Crespo, and N. Akhmediev, Dissipative Rogue Waves Generated by Chaotic Pulse Bunching in a Mode-Locked Laser, *Phys. Rev. Lett.* **108**, 233901 (2012).
- [20] J. Soto-Crespo, P. Grelu, and N. Akhmediev, Dissipative rogue waves: Extreme pulses generated by passively mode-locked lasers, *Phys. Rev. E* **84**, 016604 (2011).
- [21] D. Buccoliero, H. Steffensen, H. Ebendorff-Heidepriem, T. M. Monro, and O. Bang, Midinfrared optical rogue waves in soft glass photonic crystal fiber, *Opt. Express* **19**, 17973 (2011).
- [22] A. F. Runge, C. Aguergeray, N. G. Broderick, and M. Erkintalo, Raman rogue waves in a partially mode-locked fiber laser, *Opt. Lett.* **39**, 319 (2014).
- [23] C. Finot, K. Hammani, J. Fatome, J. M. Dudley, and G. Millot, Selection of extreme events generated in Raman fiber amplifiers through spectral offset filtering, *IEEE J. Quantum Electron.* **46**, 205 (2009).
- [24] K. Hammani, C. Finot, and G. Millot, Emergence of extreme events in fiber-based parametric processes driven by a partially incoherent pump wave, *Opt. Lett.* **34**, 1138 (2009).
- [25] N. Akhmediev, J. M. Dudley, D. R. Solli, and S. K. Turitsyn, Recent progress in investigating optical rogue waves, *J. Opt.* **15**, 060201 (2013).
- [26] Y. Song, Z. Wang, C. Wang, K. Panajotov, and H. Zhang, Recent progress on optical rogue waves in fiber lasers: Status, challenges, and perspectives, *Adv. Photonics* **2**, 024001 (2020).
- [27] M. Tlidi and M. Taki, Rogue waves in nonlinear optics, *Adv. Opt. Photon.* **14**, 87 (2022).
- [28] V. Zakharov and L. Ostrovsky, Modulation instability: The beginning, *Physica D* **238**, 540 (2009).
- [29] J. M. Dudley, G. Genty, F. Dias, B. Kibler, and N. Akhmediev, Modulation instability, Akhmediev breathers and continuous wave supercontinuum generation, *Opt. Express* **17**, 21497 (2009).
- [30] A. Gelash, D. Agafontsev, V. Zakharov, G. El, S. Randoux, and P. Suret, Bound State Soliton Gas Dynamics Underlying the Spontaneous Modulational Instability, *Phys. Rev. Lett.* **123**, 234102 (2019).
- [31] *Supercontinuum Generation in Optical Fibers*, edited by J. M. Dudley and J. R. Taylor (Cambridge University Press, Cambridge, 2010).
- [32] N. Akhmediev, A. Ankiewicz, and J. M. Soto-Crespo, Rogue waves and rational solutions of the nonlinear Schrödinger equation, *Phys. Rev. E* **80**, 026601 (2009).
- [33] S. Toenger, T. Godin, C. Billet, F. Dias, M. Erkintalo, G. Genty, and J. M. Dudley, Emergent rogue wave structures and statistics in spontaneous modulation instability, *Sci. Rep.* **5**, 10380 (2015).
- [34] A. Chowdury and W. Chang, Rogue wave fission, *Phys. Rev. Res.* **3**, L032060 (2021).
- [35] S. Randoux, P. Suret, and G. El, Inverse scattering transform analysis of rogue waves using local periodization procedure, *Sci. Rep.* **6**, 29238 (2016).

- [36] S. Randoux, P. Suret, A. Chabchoub, B. Kibler, and G. El, Non-linear spectral analysis of peregrine solitons observed in optics and in hydrodynamic experiments, *Phys. Rev. E* **98**, 022219 (2018).
- [37] F. Bonnefoy, A. Tikan, F. Copie, P. Suret, G. Ducrozet, G. Prabhudesai, G. Michel, A. Cazaubiel, E. Falcon, G. El *et al.*, From modulational instability to focusing dam breaks in water waves, *Phys. Rev. Fluids* **5**, 034802 (2020).
- [38] A. Atieh, P. Myslinski, J. Chrostowski, and P. Galiko, Measuring the raman time constant ( $t_r$ ) for soliton pulses in standard single-mode fiber, *J. Lightwave Technol.* **17**, 216 (1999).
- [39] G. P. Agrawal, Nonlinear fiber optics: Its history and recent progress [invited], *J. Opt. Soc. Am. B* **28**, A1 (2011).
- [40] V. E. Zakharov and A. B. Shabat, Exact theory of two-dimensional self-focusing and one-dimensional self-modulation of waves in nonlinear media, *J. Exp. Theor. Phys.* **34**, 62 (1972).
- [41] A. Ankiewicz and N. Akhmediev, Rogue wave solutions for the infinite integrable nonlinear Schrödinger equation hierarchy, *Phys. Rev. E* **96**, 012219 (2017).
- [42] U. Bandelow and N. Akhmediev, Persistence of rogue waves in extended nonlinear Schrödinger equations: Integrable Sasa–Satsuma case, *Phys. Lett. A* **376**, 1558 (2012).
- [43] V. B. Matveev and M. A. Salle, *Darboux Transformations and Solitons* (Springer-Verlag, Berlin, 1991).
- [44] M. Erkintalo, G. Genty, B. Wetzell, and J. M. Dudley, Akhmediev breather evolution in optical fiber for realistic initial conditions, *Phys. Lett. A* **375**, 2029 (2011).
- [45] S. Chen, F. Baronio, J. M. Soto-Crespo, Y. Liu, and P. Grelu, Chirped peregrine solitons in a class of cubic-quintic nonlinear Schrödinger equations, *Phys. Rev. E* **93**, 062202 (2016).
- [46] G. Xu, J. McNiff, A. Boardman, and B. Kibler, Space–time evolution of optical breathers and modulation instability patterns in metamaterial waveguides, *Wave Motion* **93**, 102448 (2020).
- [47] A. Boardman, A. Alberucci, G. Assanto, V. Grimalsky, B. Kibler, J. McNiff, I. Nefedov, Y. G. Rapoport, and C. Valagiannopoulos, Waves in hyperbolic and double negative metamaterials including rogues and solitons, *Nanotechnology* **28**, 444001 (2017).
- [48] G. P. Agrawal, *Nonlinear Fiber Optics*, 5th ed. (Academic Press, New York, 2012).
- [49] A. Ankiewicz, M. Bokaeeeyan, and N. Akhmediev, Rogue waves under influence of Raman delay, *J. Opt. Soc. Am. B* **35**, 899 (2018).
- [50] A. Ankiewicz, J. M. Soto-Crespo, M. A. Chowdhury, and N. Akhmediev, Rogue waves in optical fibers in presence of third-order dispersion, self-steepening, and self-frequency shift, *J. Opt. Soc. Am. B* **30**, 87 (2013).
- [51] C. Mahnke and F. Mitschke, Possibility of an Akhmediev breather decaying into solitons, *Phys. Rev. A* **85**, 033808 (2012).
- [52] C. R. Menyuk, Soliton robustness in optical fibers, *J. Opt. Soc. Am. B* **10**, 1585 (1993).
- [53] P. S. J. Russell, P. Hölzer, W. Chang, A. Abdolvand, and J. C. Travers, Hollow-core photonic crystal fibres for gas-based nonlinear optics, *Nat. Photonics* **8**, 278 (2014).
- [54] J. C. Travers, W. Chang, J. Nold, N. Y. Joly, and P. S. J. Russell, Ultrafast nonlinear optics in gas-filled hollow-core photonic crystal fibers, *J. Opt. Soc. Am. B* **28**, A11 (2011).
- [55] A. Gelash, D. Agafontsev, P. Suret, and S. Randoux, Solitonic model of the condensate, *Phys. Rev. E* **104**, 044213 (2021).
- [56] A. Chowdury, W. Chang, and M. Battiato, From rogue wave solution to solitons, *Phys. Rev. E* **107**, 014212 (2023).